Chemical Engineering Journal 156 (2010) 215–225

Contents lists available at ScienceDirect

Chemical Engineering Journal

journal homepage: www.elsevier.com/locate/cej

Computational fluid dynamic modeling of a chemical vapor synthesis process for aluminum nanopowder as a hydrogen storage precursor☆

H.Y. Sohn*, Silvia Perez-Fontes, Jin Won Choi

Department of Metallurgical Engineering, University of Utah, Salt Lake City, UT 84112, USA

ARTICLE INFO

Article history:
Received 19 August 2009
Received in revised form 9 October 2009
Accepted 16 October 2009

Keywords:
Computational fluid dynamics modeling
Chemical vapor synthesis
Nucleation and growth
Aluminum
Nanopowder
Hydrogen storage

ABSTRACT

A chemical vapor synthesis (CVS) process for synthesizing nano-sized aluminum powder as a precursor for various hydrogen storage materials was simulated by the use of computational fluid dynamic modeling. The fluid flow, heat transfer and chemical reaction phenomena taking place inside the reactor were analyzed together with particle formation and growth in the CVS process. The temperature, velocity and particle size distribution fields inside the reactor were computed. Chemical reaction rate and population balance model were used to calculate the particle formation and growth. The particle size computed by the program was compared with the experimental data, and the calculated average size of the final product particles was consistent with those obtained in the experimental work.

1. Introduction

A number of aluminum-containing compounds such as AlH_3 [1], $NaAlH_4$ [2], $LiAlH_4$ [3], and $Mg(AlH_4)_2$ [4] have been identified to have high potentials as hydrogen storage materials, especially for automotive application. Sohn and coworkers [5,6] have prepared nano-sized aluminum powder by a chemical vapor synthesis (CVS) process. Chemical vapor synthesis is a method for preparing solid powders by vapor-phase reactions and provides considerable flexibility in producing nano-materials by the use of wide variety of precursors. The CVS process involves reducing a vapor-phase mixture of volatile precursors of the constituent metals by magnesium vapor or hydrogen, depending on the thermodynamics of the synthesis reactions. The key advantages of this process are small product particle size, the ability to produce powders of many different compositions, the homogeneity of powder composition, and the ease of dopant addition in one-step synthesis. The precursors can be solids, liquids or gases at ambient conditions, but they are delivered to the reaction location as a vapor from a bubbler or volatilization source, as necessary.

Another key feature of chemical vapor synthesis is that it allows the formation of uniformly mixed multi-component nanoparticles through the use of multiple precursors. Sohn and coworkers [5] synthesized WC–Co composite powder by reducing WCl_6 and $CoCl_2$ precursors. Srdic et al. [7] prepared zirconia particles doped with alumina by oxidizing liquid precursors, zirconium-t-butoxide (ZTB) and aluminum-s-butoxide (ASB) in two sequential tubular reactors. Sohn and Paldey [8–11] used the CVS to prepare nickel and titanium aluminides and molybdenum nikelide by reducing mixtures of metal chlorides with hydrogen or magnesium in the vapor phase.

The synthesis of aluminum nanopowder by the vapor-phase reduction of aluminum chloride with magnesium is represented by:

$$AlCl_3(g) + 3/2Mg(g) = Al(l, s) + 3/2MgCl_2(g) \quad (1)$$

Experimental results involving the CVS process have shown that mixing ratio and mixing patterns of the vapor-phase reactants are important parameters that affect nanoparticle synthesis kinetics and morphology. In addition, residence time, location of reactant feeders and temperature influence the product particle size [5,12,13]. However, it is difficult to experimentally quantify the relationship between these factors and the physical properties of the product particles. To better understand the effects of these

☆ *Disclaimer*: This report was prepared as an account of work sponsored by an agency of the United States Government. Neither the United States Government nor any agency thereof, nor any of their employees, makes any warranty, express or implied, or assumes any legal liability or responsibility for the accuracy, completeness, or usefulness of any information, apparatus, product, or process disclosed, or represents that its use would not infringe privately owned rights. Reference herein to any specific commercial product, process, or service by trade name, trademark, manufacturer, or otherwise does not necessarily constitute or imply its endorsement, recommendation, or favoring by the United States Government or any agency thereof. The views and opinions of authors expressed herein do not necessarily state or reflect those of the United States Government or any agency thereof.

* Corresponding author at: Department of Metallurgical Engineering, University of Utah, 135 South 1460 East, Room 412, Salt Lake City, UT 84112-0114, USA. Tel.: +1 801 581 5491; fax: +1 801 581 4937.
E-mail address: h.y.sohn@utah.edu (H.Y. Sohn).

1385-8947/$ – see front matter © 2009 Elsevier B.V. All rights reserved.
doi:10.1016/j.cej.2009.10.044

Nomenclature

c.v.	coefficient of variation (ratio of standard deviation to mean)
C_i	molar concentration of species i (kmol/m^3)
C_p	heat capacity (J/kg K)
d_p^*	critical particle size for nucleation (nm)
D_i	molecular diffusivity of species i (m^2/s)
G	particle growth rate (m/s)
g_z	gravitational acceleration (m/s^2)
h_i	enthalpy of species i (J/kg)
J	particle nucleation rate (#/m^3 s)
$\vec{j}_i$	diffusive mass flux of species i (kg/m^2 s)
k	thermal conductivity (W/m K)
k_B	Boltzmann's constant (J/K)
k_g,	particle growth rate constant (m^4/kmol s)
k_n	particle nucleation rate constant (m^3/mol s)
k_m	mass transfer coefficient (m/s)
L	particle diameter (nm)
m_i	ith moment of particle number density function (m^{i-3})
M_i	molecular weight of species i (kg/kmol)
n, $n(L)$	particle number density function (#/m^4)
$\vec{n}_i$	mass flux vector of species i (kg/m^2 s)
N_A	Avogadro's number (#/kmol)
p_1	partial pressure of species 1 (Pa)
p_e	equilibrium vapor pressure over a flat surface (Pa)
P	pressure (Pa)
$\vec{q}$	conductive heat transfer vector (J/m^2 s)
R_j	rate of jth reaction (kmol/m^3 s)
R_s	molar rate of aluminum deposition to the particle per unit area (kmol/m^2 s)
S	saturation ratio, $S = p_1/p_e$
S_m	source term for mass added to the gas phase by reaction involving condensed phase (kg/m^3 s)
T	temperature (K)
v_1	molecular or atomic volume (m^3)
$\vec{v}$	gas velocity vector (m/s)
v_x, v_y, v_z	gas velocity components in x, y, z directions (m/s)
V_{mol}	molar volume (m^3/kmol)
Y	gas-phase species mass fraction (kg/kg)

Greek symbols

μ	molecular viscosity (kg/m s)
$\nu_{i,j}$	stoichiometry coefficient of species i in jth reaction
ρ	mass density (kg/m^3)
σ^2	variance (square of standard deviation) (m^2)
$\vec{\tau}_x$, $\vec{\tau}_x$, $\vec{\tau}_x$	flux vectors of momentum in the x, y, z directions (N/m^2)
$\dot{\omega}_i$	net generation of species i by homogenous chemical reactions (kmol/m^3 s)

factors, a mathematical model was developed and solved using a commercial CFD computer program Fluent. The results of simulation were used to identify the relationships between particle properties and gas flow pattern in the reactor.

2. Computational fluid dynamics model formulation

In computational fluid dynamics (CFD) modeling, the simulation of fluid flow makes it possible to analyze the flow characteristics in realistic geometries and makes it easier to improve process and reactor designs. Based on the integration of the principles of transport phenomena and chemical reaction kinetics, the CFD simulation can be used for determining optimum reactor configurations and conditions, such as reactant feed rates and the locations of feeder inlets to control particle size and maximize the product yield of the powder.

Table 1
Gas-phase governing equations.

Overall continuity	$\vec{\nabla}\cdot\rho\vec{v} = S_m$	(2)
Momentum in x direction	$-\vec{\nabla}\cdot(\rho v_x\vec{v}) - \vec{\nabla}\cdot\vec{\tau}_x - \frac{\partial P}{\partial x} = 0$	(3)
Momentum in y direction	$-\vec{\nabla}\cdot(\rho v_y\vec{v}) - \vec{\nabla}\cdot\vec{\tau}_y - \frac{\partial P}{\partial y} = 0$	(4)
Momentum in z direction	$-\vec{\nabla}\cdot(\rho v_z\vec{v}) - \vec{\nabla}\cdot\vec{\tau}_z - \frac{\partial P}{\partial z} + \rho g_z = 0$	(5)
Energy	$-\rho\vec{v}\cdot C_p\vec{\nabla}T - \vec{\nabla}\cdot\vec{q} - \sum_{i=1}^{n} h_i M_i\dot{\omega}_i = 0$	(6)
Continuity of species i	$-\vec{\nabla}\cdot\vec{n}_i + M_i\dot{\omega}_i = 0$	(7)
Net mass flux of species i	$\vec{n}_i = \rho_i\vec{v} + \vec{j}_i$	(8)
Diffusive mass flux of species i	$\vec{j}_i = -\rho D_{im}\vec{\nabla}Y_i$	(9)
Net generation of species i by surface chemical reactions	$\dot{\omega}_i = \sum_{j=1}^{J} v_{i,j}R_j$	(10)

Table 2
Equations for gas-phase transport properties.

Mixture viscosity	$\mu_m \approx \mu_{Ar} = 2.6693\times10^{-6}\frac{\sqrt{M_{Ar}T}}{\sigma^2\Omega_\mu}$	(11)
Mixture thermal conductivity	$k_m \approx k_{Ar} = 8.3279\times10^{-2}\frac{\sqrt{T/M_{Ar}}}{\sigma^2\Omega_k}$	(12)
Species Fickian diffusivity	$D_{im} \approx D_{iAr} = 1.8829\times10^{-2}\frac{\sqrt{T^3}}{P\sigma_{iAr}^2\Omega_D}\left(\frac{1}{M_i}+\frac{1}{M_{Ar}}\right)$	(13)

2.1. Basic fluid-phase equations

The commercial CFD code FLUENT uses conservation equations for mass and momentum combined with an equation for energy conservation to describe heat transfer phenomena. Table 1 shows the basic steady state governing equations used in this simulation.

Eq. (2) in Table 1 represents the total mass conservation equation and Eqs. (3)–(7) describe the components of the gas velocity (v_x, v_y and v_z), the gas temperature (T) and the gas-phase species mass fraction (Y), respectively, as functions of position inside the reactor.

Table 2 shows the expressions used to compute the gas-phase transport properties. Because the reactants are mixed in large excess Ar throughout the reactor, the viscosity and thermal conductivity of the gas mixture were set to those of pure Ar. Similarly, the Fickian diffusivities of the gas-phase species were set to the binary values of those species in Ar. The gas phase was assumed to obey the ideal-gas law.

2.2. Particle population balance

The development of most population balance models begins with the general dynamic equation (GDE) in terms of particle number density function. By solving the GDE for different initial and boundary conditions, the particle size distribution function can be obtained. The GDE represents a population balance of the particles in a volume element, which at steady state is given by the following

equation [14]:

$$\frac{\partial}{\partial L}(nG) + \nabla \cdot (n\vec{v}) = Birth - Death \quad (14)$$

where n is the particle number density function. The birth and death source terms represent the rates of particles birth and death due to aggregation and other related phenomena. The boundary condition at $L = 0$ for the integration of the first term of Eq. (14) is obtained from

$$ndL|_{L=0} = Jdt = J\left(\frac{dL}{G}\right) \quad (15)$$

$$n(0, \vec{x}) = \frac{J}{G|_{L=0}} \quad (16)$$

where J represents the rate of nucleation of particles.

When the gas phase is sufficiently supersaturated, particles nucleate and grow. A multiphase model is necessary to model the particle nucleation and growth in Fluent. The Mixture and Eulerian models are generally used for the multiphase modeling [15]. In this research, the Mixture model provided in the Fluent code was used because it is simple and requires less computational work, while the accuracy is acceptable.

2.3. Modeling particle nucleation and growth

The determination of the nucleation and growth kinetics for aluminum particles produced from the reduction reaction is a difficult problem because the reaction occurs in the gas phase and is extremely fast. Therefore, it is difficult to obtain the information experimentally. Many researchers have investigated the particle nucleation and growth rate by modeling [14,16,17]. However, they focused on modeling the physical evaporation and condensation process by volatilizing bulk aluminum.

Simplified general expressions have been used for the nucleation and growth rates, together with assumed values of the rate parameters, which were successfully applied for SiO_2 nanoparticle simulation [18,19]. The kinetic parameters for the nucleation and growth were treated as adjustable parameters and the best set of the values by comparing the results with the experimental data were determined in this previous work.

Gas-phase homogenous nucleation is a process by which gas atoms or molecules are transformed into liquid or solid particles. For a supersaturated vapor, clusters form but most of them are thermodynamically unstable with respect to evaporation. Only the sufficiently large clusters are thermodynamically stable. The Kelvin effect describes the stability of the atomic clusters and particles with respect to evaporation [20]. The Kelvin effect is expressed by

$$d_p^* = \frac{4\sigma v_1}{k_B T \ \ln S} \quad (17)$$

where σ (N/m) is the surface tension. The parameters used for the Kelvin diameter calculation are presented in Table 3. If the critical particle size d_p^* is smaller than the monomer size, the nucleation is considered as collision-controlled nucleation because there is no thermodynamic barrier for nucleation. The calculated value of d_p^* for aluminum was 0.217 nm, smaller than the monomer diameter (0.286 nm). Thus, the monomer is thermodynamically stable and there is no thermodynamic barrier to the formation of the aluminum particles. In this case, each atom or molecule is a particle from the thermodynamic point of view. It means that the growth of the clusters is not inhibited by thermodynamics and becomes collision limited.

In cases where chemical reaction occurs to form the monomer and when the critical size is smaller than the monomer size, nucleation is equivalent to chemical reaction in the sense that each product molecule forms a monomer. This condition occurs for many materials produced at low temperatures relative to their melting points [20].

Based on the theory of chemical reactions, the nucleation rate is expressed by

$$J = k_n N_A C_a C_b \quad (18)$$

where J (#/s m^3) is the nucleation rate and k_n (m^3/kmol s) represents the rate constant. In this work, J was set equal to zero when temperature was less than 1073 K for purely computational reasons because Fluent has difficulty in numerically handling very low nucleation rates due to low temperatures or reactant concentrations.

The gaseous reactant is transported to the particle surface where reactions take place to form the product particles. The rate of the surface reaction involving the two gaseous reactants $AlCl_3$ and Mg is represented by

$$R_s = k_g C_{AlCl_3} C_{Mg} \quad (19)$$

where R_s is the molar rate of aluminum deposition to the particle per unit area (kmol/m^2 s), k_g is the surface reaction rate constant (m^4/kmol s). The volumetric growth rate of the particle is then given by:

$$\frac{dv}{dt} = R_s \pi d_p^2 V_{mol} \quad (20)$$

where d_p is the particle diameter (m) and V_{mol} is the molar volume of the aluminum particle (m^3/kmol). The growth rate of particle diameter is obtained, as follows:

$$G_{rxn} = \frac{dd_p}{dt} = 2R_s V_{mol} \quad (21)$$

For the reaction of $AlCl_3$(g) and Mg(g) to form Al on the particle, G_{rxn} (m/s) becomes

$$G_{rxn} = 1.48 \times 10^{-2} \ k_g C_{AlCl_3} C_{Mg} \quad (22)$$

The linear growth rate of a particle under the control of mass transfer G_{mass} is determined by the smaller of the mass transfer

Table 3
Parameters used for calculation of the Kelvin diameter.

Parameter	Value	Ref.
Surface tension, $\sigma = (948–0.202T)/1000$	0.69 (N/m)	[21]
Atomic volume of Al, v_1	1.23×10^{-29} (m^3)	
Temperature, T	1273 (K)	
Total pressure, P	101.3 kPa	
Total Ar flow	12.4 L/min (25 °C, 86.1 kPa)	
Aluminum concentration per unit mass of gas[a], n_m	2.043×10^{22} (#/kg)	
Vapor pressure, $p_e = \exp(13.07 - 36373/T)P$	0.0187 (Pa)	[22]
Saturation concentration of aluminum, $n_{ms} = p_e/k_B T$	1.067×10^{18} (#/m^3)	
Carrier gas density, $\rho_g = PM_w/RT$	0.382 (kg/m^3)	
Super saturation ratio, $S = p_1/p_e = n_m/(n_{ms}\rho_g)$	7292	

[a] Assuming all $AlCl_3$ (0.00075 mol/min) reacted and converted to Al.

rate of $AlCl_3$ or Mg, represented by the following expressions the derivation of which is shown in Appendix C:

$$G_{m,\,AlCl_3} = 4V_{mol}D_{AlCl_3}\frac{m_0}{m_1}C_{AlCl_3,b} \tag{23a}$$

and

$$G_{m,\,Mg} = \frac{8}{3}V_{mol}D_{Mg}\frac{m_0}{m_1}C_{Mg,b}. \tag{23b}$$

The overall growth rate G_t is expressed by combining the rates under the control of mass transfer and chemical reaction kinetics as follows [23]:

$$\frac{1}{G_t} = \frac{1}{G_{rxn}} + \frac{1}{G_{mass}} \tag{24}$$

This expression, which is exact for processes whose rates have first-order dependence on concentration, has been shown to be valid at least approximately for other cases [24]. Further, it becomes exact when $G_{rxn} \gg G_{mass}$ or $G_{rxn} \ll G_{mass}$, which is often the case. In this work, G_t was set equal to zero when $T \leq 1073$ K. Again, this was done for the same numerical reasons as described above in conjunction with the nucleation rate expression.

The particle size distribution characteristics are expressed in terms of the appropriate moments of the size distribution. The ith moment m_i is defined by [25]

$$m_i = \int_0^\infty L^i n(L)dL \tag{25}$$

where L is the particle size and $n(L)$ is the particle number density function. The zeroth moment, m_0 represents the total number of particles per unit volume of the gas-particle mixture. The first moment, m_1, represents the total length of particles per unit volume. The second moment, m_2, represents the total surface area of particles per unit volume. The third moment, m_3, represents the total volume of particles per unit volume.

The GDE is normally coupled with the gas-phase equations such as momentum, heat and chemical equations. The GDE is a nonlinear, partial integro-differential equation. When complicated reactor geometries or boundary conditions are to be incorporated, analytical solutions are not possible. Therefore, many efforts have been made to develop numerical tools to solve it efficiently and accurately. In this research, commercial fluid dynamic program Fluent was used as the solver for the computation of the CVS process. The Quadrature Method of Moments (QMOM) [26], which is a numerical solution method for population balance models, was used to solve the GDE.

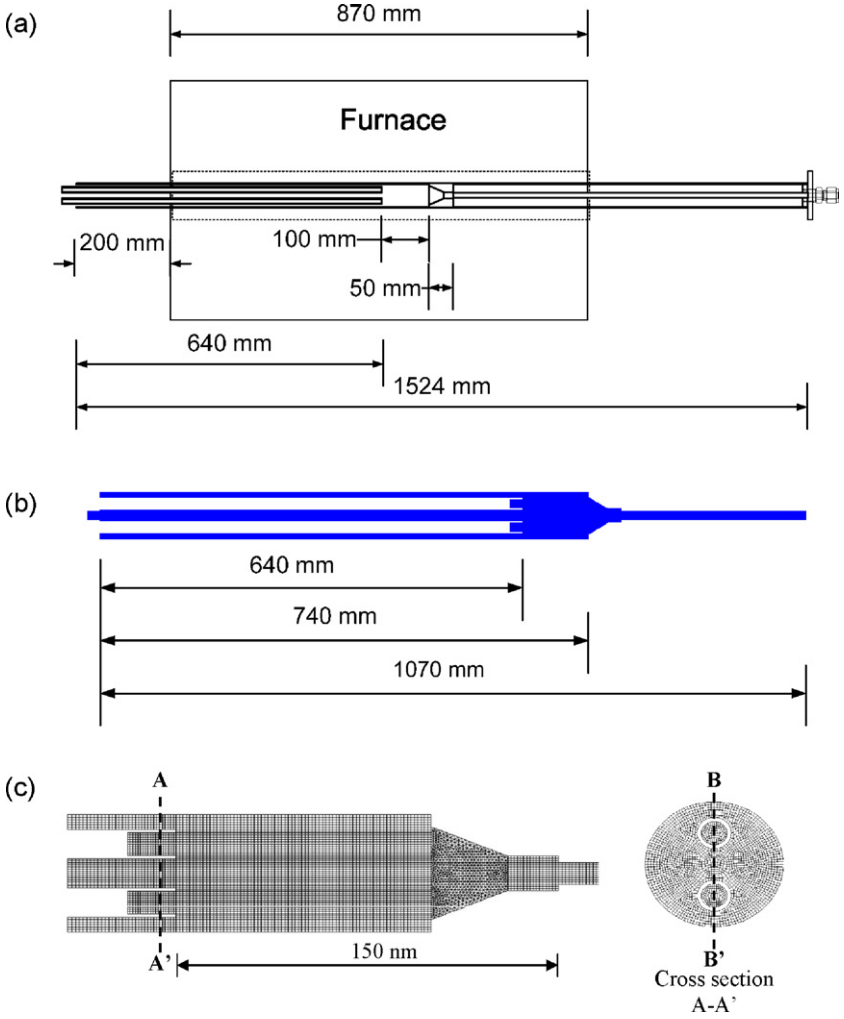

Fig. 1. Geometry of the reactor for simulation: the left side of the figures represents the inlet for the precursors while the right side represents the outlet of the mixture gas. (a) Actual geometry, (b) geometry used for simulation, and (c) magnified view of mesh design.

2.4. Geometry for simulation and assumptions

The details of the experimental apparatus in which Al nanopowder was synthesized are shown in Figs. A1–A3 of Appendix A. These figures show, among other features, the geometries of the feeding tubes for reactant powders and the Ar gas. The temperature of the reactor wall was measured using a K-type thermocouple and used for the simulation. The measured wall temperature profiles for the two different furnaces set at 1000 °C and 1200 °C are shown in Fig. B1 of Appendix B. The length of the constant temperature zone was around 50 cm. The measured wall temperature reached the target temperature except for the 20 cm lengths from the inlet and the outlet. It showed a long hot zone with a uniform wall temperature in the reactor, because the 3-zone heating element in the furnace provided precise temperature control. The spatial variation of the wall temperature in the hot zone was about 10 °C. After the hot zone, the wall temperature cooled down rapidly.

For the simulation, only the part of the actual reactor from the Ar inlet to the furnace outlet was considered so that the simulation time and complexity of designing the model may be reduced. Fig. 1(a) indicates actual geometry of the system and (b) shows the geometry used for simulation. The left side of the figures represents the inlet for the precursors while the right side represents the outlet of the mixture gas. The experiments were performed at steady state. The product particles were considered spherical and agglomeration of the particles was not considered because the particle growth involves a number of rather complicated mechanisms, and thus in this study, the particle growth rate constant was treated as an adjustable parameter. Therefore, the growth mechanisms, except the well defined mass transfer step, were combined into the growth rate constant.

GAMBIT 2.2.30 was used for mesh generation. Three-dimensional meshes were created for the reactor used in the experiments. The entire domain was 1070 mm in length and 50 mm in diameter. The number of cells for the simulation was 412,155. The mesh design is shown in Fig. 1(c).

3. Results and discussion

The conditions for the standard experimental runs are presented in Table 4, in which the various Ar streams correspond to those described in Fig. A2 in Appendix A. The total Ar flow rate is the sum of the carrier Ar, additional carrier Ar and dilution Ar flow rates. The heating of the gas in the feed tube was simulated by separate CFD modeling which indicated that the gas exited the tube at 800 °C. Thus, the carrier Ar temperature at the feed tube was set at this temperature and the feeding tube was excluded from the overall reactor simulation to reduce the computational complexity. Unless otherwise specified, the results of the simulation presented below are for the standard conditions given in Table 4.

The solution was converged after some 2000 iterations. Convergence was defined when the residuals, defined by the absolute value of the difference between successive iterations, of all the variables reached the user-defined value, typically 10^{-5} to 10^{-6}. It took more than 6 h of computation for one run of this 3D model on a computer with a dual-core-type 3.0 GHz processor and 4 GB RAM memory.

3.1. Velocity distribution

The velocity distribution inside the reactor affects the properties of the final product because it transports particles by convection throughout the reactor. In Eq. (14) that describes the change in the particle size distribution, the convection term is a function of the gas velocity. The flow field calculated for the standard set of conditions is presented in Fig. 2 which shows the cross-sectional view passing through the B–B′ plane as shown in Fig. 1(c) from the injection tube to the end of the furnace.

Table 4
Operating conditions for the simulation.

	Parameter	Value
System	Environment	Argon
	Precursors	$AlCl_3$, Mg
Carrier Ar[a]	Flow rate	1 L/min each tube (25 °C, 86.1 kPa)
	Temperature	800 °C[b]
Additional carrier Ar[a]	Flow rate	0.3 L/min each tube (25 °C, 86.1 kPa)
	Temperature	25 °C
Dilution Ar[a]	Flow rate	8 L/min (25 °C, 86.1 kPa)
	Temperature	25 °C
Total Ar flow[a]	Flow rate	10.6 L/min (25 °C, 86.1 kPa)
Precursor[c]	Precursor feeding rates	$AlCl_3$: 0.1 g/min
		Mg: 0.03 g/min
Furnace	Wall temperature	1000 °C

[a] The different Ar streams mentioned in this table correspond to those described in Fig. A2 in Appendix A.
[b] Based on simulation including the precursor feeding tubes carried in the earlier stage, the temperatures of the tubes were 800 °C. After this, the temperature was assumed to be 800 °C in all cases to reduce the calculation time. Further, the radial variation of this temperature was negligible because of the small diameter.
[c] Solid precursors were fed by specially designed powder feeders described in Ref. [6]. These precursors were rapidly volatilized when they entered the reactor.

The color scale indicates the magnitude of the velocity field. The velocity of dilution Ar inlet, $AlCl_3$ and Mg inlet are 1.45, 0.864 and 0.874 m/s, respectively. The velocity in the area after the graphite funnel, installed to increase gas phase mixing, has the highest value of 17.8 m/s due to the reduced gas passage area.

3.2. Temperature distribution

The measured wall temperature profile described in Fig. B1 in Appendix B was used as a boundary condition for the simulation. The two-dimensional temperature distribution inside the reactor is presented in Fig. 3. The distribution is based on the cross-sectional

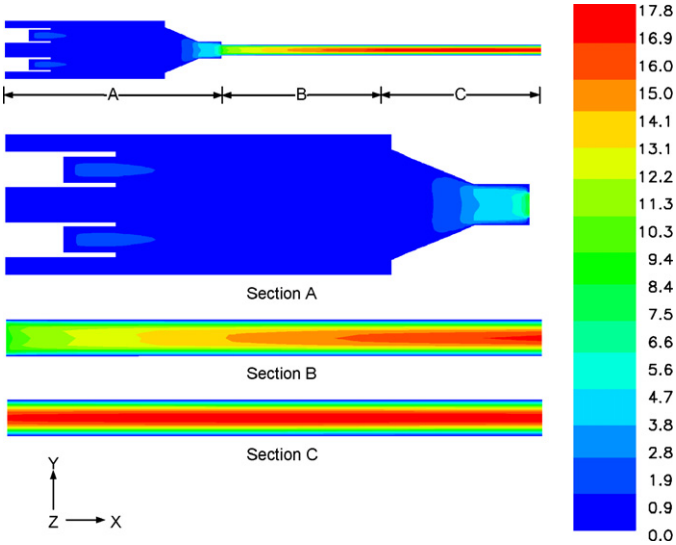

Fig. 2. Contours of velocity magnitude along the B–B′ plane in Fig. 1 (mixture, m/s) for the standard conditions given in Table 4.

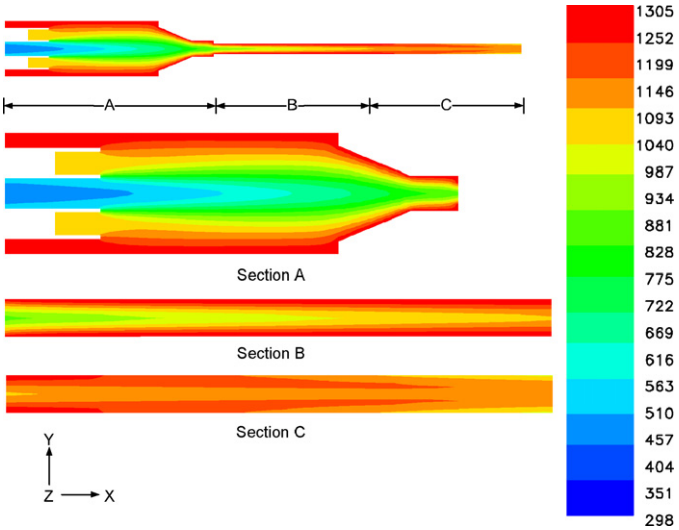

Fig. 3. Contours of gas temperature along the B–B′ plane in Fig. 1 (K) for the standard conditions given in Table 4.

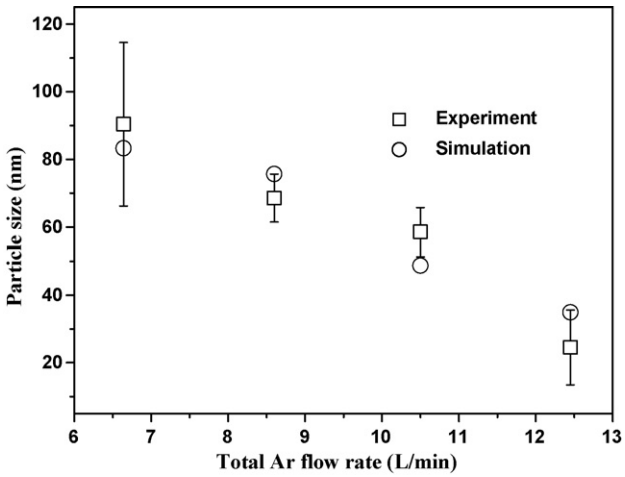

Fig. 4. Comparison of the computed and experimental average particle sizes for various total Ar flow rates.

view passing through the B–B′ plane in Fig. 1(c) from the injection tube to the end of the furnace. The wall of the reactor is at a constant temperature of 1273 K in most part, while the dilution Ar gas enters the reactor at 298 K. The temperature of the gas in the precursor injection tube increases rapidly because of the heat transfer from the wall. At the center of the reactor (in front of the graphite tube), the gas phase is mixed and thermal boundary layers are developed along the streamlines. After the graphite funnel, the temperature of the gas mixture increases due to the heat transfer from the tube wall which has a small diameter. The temperature after the funnel tube gradually decreased after reaching the maximum temperature of 1167 K. The average temperature of the reactor exit was around 773 K.

3.3. Particle kinetic constants

The rate parameters for nucleation and particle growth for the synthesis of aluminum particles from magnesium reduction of $AlCl_3$ in the vapor phase are unknown. Further, it would be extremely difficult to obtain them experimentally. In this research, the simulation was based on the determination of the best values of nucleation rate constant k_n and particle growth rate constant k_g, respectively, in Eqs. (18) and (22) by comparing the computed results with available experimental data. Each of these rate constants contains activation energy and pre-exponential factor, making it extremely difficult to estimate all of them from the experimental data. Based on the fact that the product $MgCl_2(g)$ starts appearing well into Section C of the narrow reaction tube (as shown in Fig. 7) by which point the temperature has reached a uniform value of 873 °C (1146 K), which lasted until the end of the reaction zone, as shown in Fig. 3, a constant value of k_g was assumed. On the other hand, when a best fit constant value for k_n was assumed most nucleation occurred at the entrance of the funnel, at the axial position of 730–750 mm from the left end of the reactor (Fig. 1), as shown in Fig. 13. In this zone, the temperature along the centerline, where the two gaseous reactants come into contact is 555 °C (828 K) as seen in Fig. 3. Thus, the constant value of k_n corresponds to its value at this temperature. The average particle size measured by ZetaPALS, as described below, was 58 nm under the experimental conditions of $AlCl_3$ 0.1 g/min, Mg 0.03 g/min, and total Ar flow 10.6 L/min (25 °C, 86.1 kPa average barometric pressure at Salt Lake City). The average particle size decreased as the total Ar flow rate increased. Various combinations of nucleation and growth rate constants were tested, and the optimum values that gave the best fit with all the experimental data were determined. Table 5 presents the average particle sizes at the outlet computed with several sample combinations of the nucleation rate constant k_n and particle growth rate constant k_g, when the total Ar flow rate was 10.6 L/min (25 °C, 86.1 kPa). The combinations of rate constants tested included values of k_n other than 0.01 m^3/kmol s shown in this table, but the best results were obtained with this value of k_n. The average size was calculated from the value of m_1/m_0 that describes the average particle size based on the total length of the particles diameter divided by the number of particles, i.e. the number-average size and the particles were considered to be spherical. In the analysis of ZetaPALS, the nanoparticles will scatter incoming laser light. Due to the random motion of these particles, the scattered light intensity fluctuates in time. The fluctuating signal is processed and the equivalent spherical particle size is calculated using the Stokes–Einstein equation. The calculated average particle size and distribution from the ZetaPALS are number-averaged particle sizes, which was the reason to calculate a number-average size in the simulation.

Fig. 4 shows the comparison of the simulation results with experimental particles size as a function of total Ar flow rate, which was varied by changing the dilution Ar flow rate defined in Table 4 and Appendix A while keeping all other conditions the same. The set of $k_n = 1 \times 10^{-2}$ (m^3/kmol s) and $k_g = 2.25 \times 10^5$ (m^4/kmol s) showed the best overall agreement with the experimental results with all the Ar flow rates tested. With this value of k_g, G_{rxn} is much smaller than G_{mass} by a ratio of 10^{-4}–10^{-3}, indicating that chemical reaction, not mass transfer, is the controlling step in particle growth in this system where very small particles are produced. This is because

Table 5
Computed average particle size with various k_n and k_g.

k_n (m^3/kmol s) at an average temp. of 555 °C (828 K)	k_g (m^4/kmol s) at an average temp. of 873 °C (1146 K)	Average particle size, m_1/m_0 (nm)
0.01	2.25×10^5	48.9
0.01	3.59×10^5	64.4
0.01	8.98×10^5	99.6

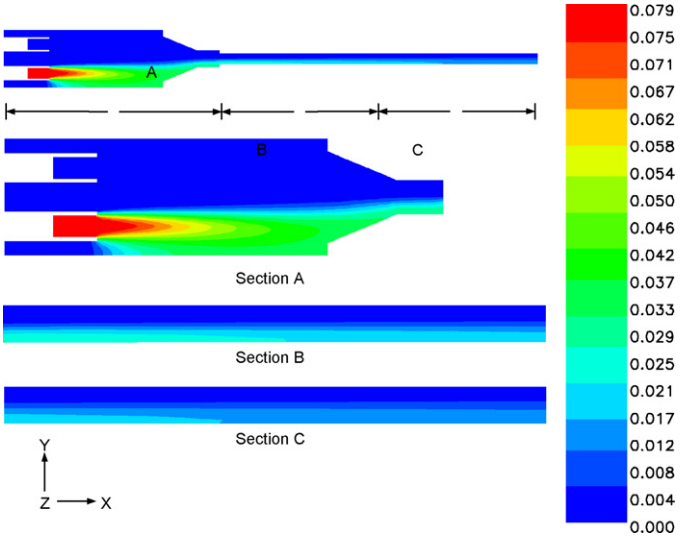

Fig. 5. Contours of mole fraction of $AlCl_3(g)$ along the B–B′ plane in Fig. 1 for the standard conditions given in Table 4.

mass transfer to these small particles is even faster that the rapid chemical reaction.

The vertical lines around the experimental points represent the standard deviations obtained from five repeated experiments and the open squares are the average particle sizes. The simulation results showed a reasonable agreement with experimental results within 10 nm error range.

3.4. Concentration distributions

As described earlier, the mixing characteristics of the precursor are another important factor. Figs. 5–7 show the concentration profiles of the species in the reactor. $AlCl_3$ and Mg vapor enter from the injector tubes and the dilution Ar gas stream prohibits the mixing of the precursors by separating the streams of $AlCl_3(g)$ and Mg(g), thus preventing premature nucleation. However, the graphite funnel reduces the flow area, by which the mixing path in the radial direction decreases, facilitating the gas-phase reaction. The $MgCl_2(g)$ concentration starts increasing after the graphite funnel indicating the start of the reduction reaction between $AlCl_3(g)$ and Mg(g).

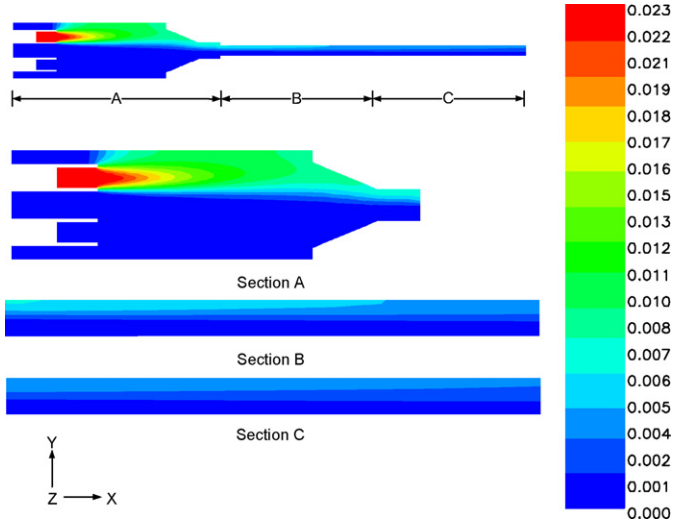

Fig. 6. Contours of mole fraction of Mg(g) along the B–B′ plane in Fig. 1 for the standard conditions given in Table 4.

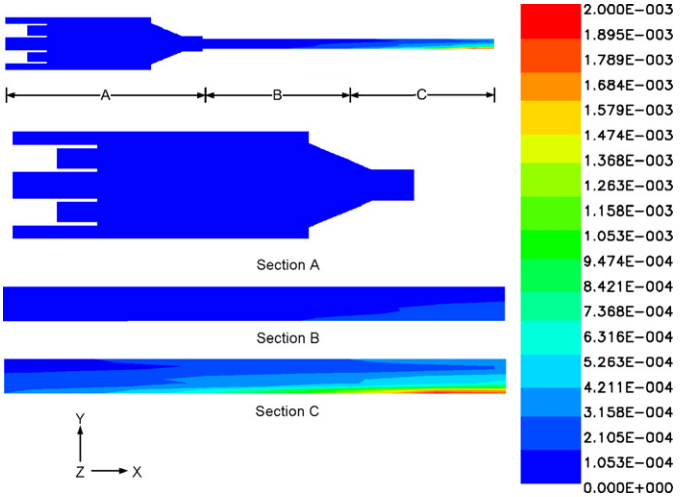

Fig. 7. Contours of mole fraction of $MgCl_2(g)$ along the B–B′ plane in Fig. 1 for the standard conditions given in Table 4.

3.5. Average particle size (APS)

The profile of average particle size (APS) is presented in Fig. 8. The APS is affected by nucleation and growth. Most nucleation takes place at the entrance of the funnel, and thereafter the particles grow by surface reaction on the existing particles in the narrow part of the reactor tube due to the reduced area which promotes gas phase mixing. The distribution of the APS at the outlet is given in Fig. 9. Near the wall, the average particle size is large because the velocity is lower there, which promotes particle growth. However, most of the particles at the outlet were less than 50 nm.

3.6. Coefficient of variation

The third parameter used to describe the evolution of the particle size distribution along the reactor is the spread. To describe the spread of the particle size distribution, the coefficient of variation (c.v.) was used. When comparing between distributions with

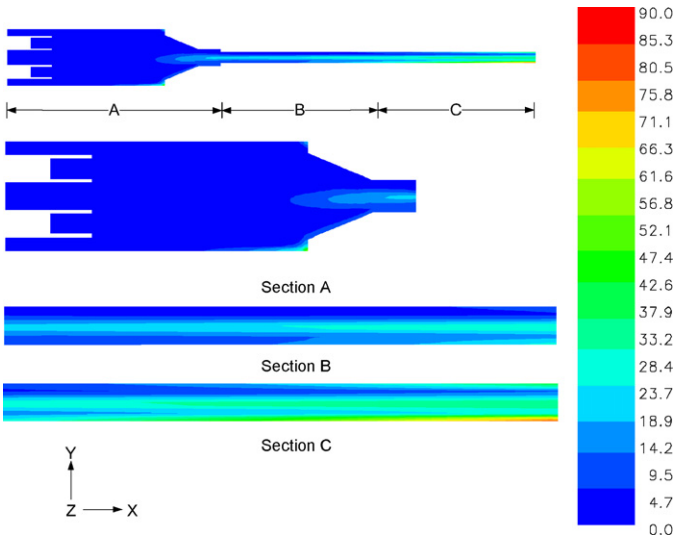

Fig. 8. Contours of average particle size along the B–B′ plane in Fig. 1 (m_1/m_0, nm) for the standard conditions given in Table 4.

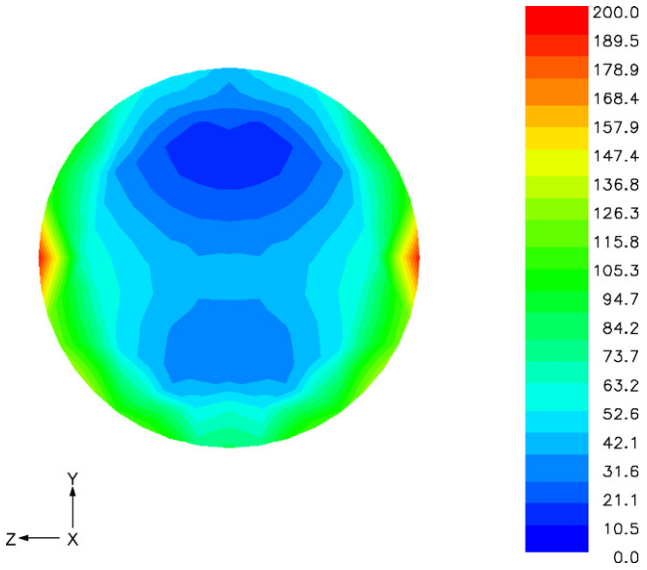

Fig. 9. Contours of average particle size at the outlet (m_1/m_0, nm) for the standard conditions given in Table 4.

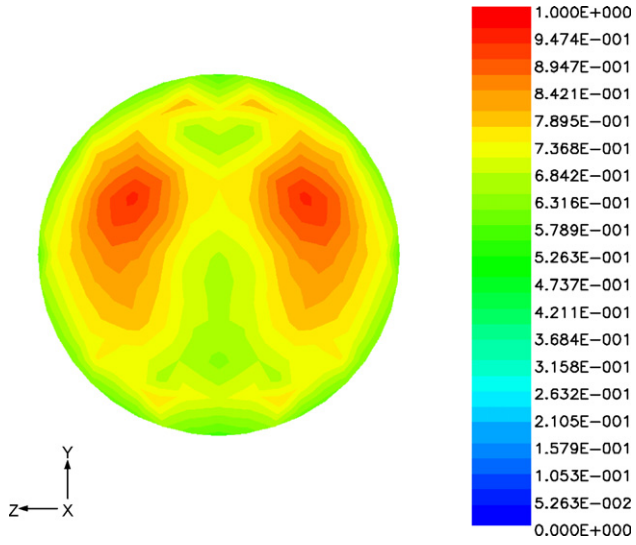

Fig. 11. Contours of c.v. value at the outlet for the standard conditions given in Table 4.

considerably different means, the coefficient of variation is advantageous over the standard deviation. Since the c.v. value represents the ratio of the standard deviation to the mean, it is a useful parameter for comparing the degree of variation for different reactor configurations and operating conditions, especially when the means are greatly different from each other. The mean and variance are given by:

$$\bar{L} = \frac{\int_0^\infty L \cdot n(L)dL}{\int_0^\infty n(L)dL} = \frac{m_1}{m_0} \tag{26}$$

$$\sigma^2 = \frac{1}{m_0}\int_0^\infty (L-\bar{L})^2 f(L)dL \tag{27}$$

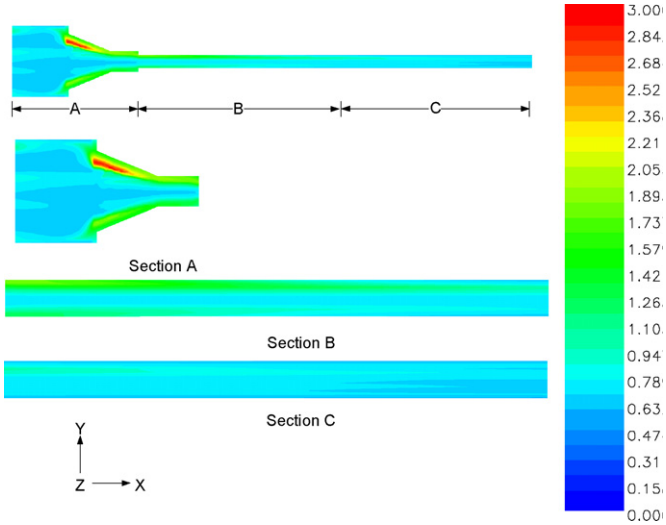

Fig. 10. Contours of c.v. value along the B–B′ plane in Fig. 1 for the standard conditions given in Table 4.

The equation can be rearranged in terms of the moments of the distribution to give

$$\sigma^2 = \frac{m_2}{m_0} - \frac{m_1^2}{m_0^2} \tag{28}$$

Thus c.v. is given in terms of the moments as

$$\text{c.v.} = \frac{(m_2/m_0 - m_1^2/m_0^2)^{1/2}}{m_1/m_0} = \left(\frac{m_0 m_2}{m_1^2} - 1\right)^{1/2} \tag{29}$$

The profile of this parameter calculated from the simulation is presented in Fig. 10. At the entrance of the funnel, new particles start to form and the spread is relatively large near the wall side because the velocity is relatively low. The small tube is the place where the growth of particles takes place. Therefore, the c.v. value decreases to less than 1, narrowing the relative spread of the particle size distribution. However, there is a variation along the small tube wall side. The wall side has relatively low velocity due to the boundary layer of the flow, which increases c.v. value. But the c.v. value decreases along the reactor length and reaches a value less than 1. The radial distribution of the c.v. at the outlet is presented in Fig. 11. Again, the radial distribution becomes rather even at the reactor exit. The c.v. value at the outlet was 0.6–0.9.

The computation of the profile of c.v. values is a valuable tool in determining the reactor configurations and operating conditions that will eliminate regions of large variations in particle size.

3.7. Particle number density

Although the axial contours are not shown, the particle number density increases along the centerline from zero to about $3 \times 10^{13}\ \text{m}^{-3}$ at the entrance of the funnel and gradually increases up to about $1.1 \times 10^{14}\ \text{m}^{-3}$ in the small tube. The radial particle number density distribution of the aluminum particles at the outlet is presented in Fig. 12. The particle number density near the wall is higher than that at the center, because the velocity which promotes the reaction is lower near the wall, providing more time for the formation of particles from the gas-phase reaction.

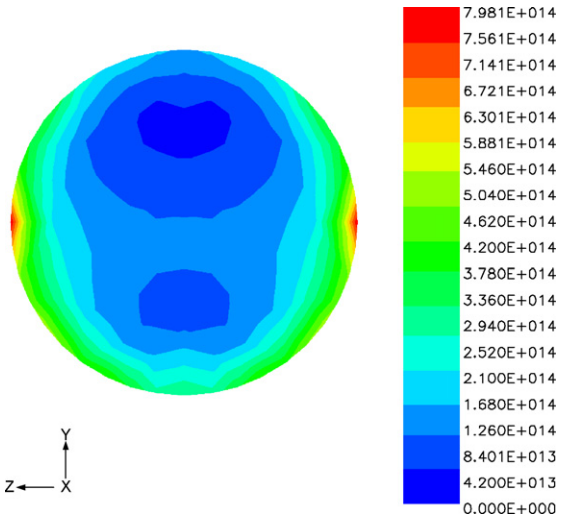

Fig. 12. Particle number density in radial direction at the outlet (#/m^3) for the standard conditions given in Table 4.

3.8. Effect of total Ar flow rate on the profiles of number density and particle size

An increase in the total Ar flow rate reduces the concentration of the gas phase in the reactor, leading to a reduced particle nucleation. Fig. 13 shows the effect of the total Ar flow rate on the particle number density along the reactor centerline. At the precursor injection tube, the aluminum number density is zero. A near linear increase in the particle number density after the funnel can be observed in this figure. The number density of aluminum particles at lower flow rates is greater than for higher flow rates. The number density increases right before the funnel (at 0.64–0.74 m), decreases in the funnel (at 0.74–0.79 m) by the addition of converging carrier gases for the reactants, and gradually increases thereafter (at ~1.07 m). However, in the higher flow rates, the particle number density increases monotonically past the funnel area. This is because higher Ar flow rates decrease the concentration of the gas species in the reactor and the nucleation of the particles was inhibited before the funnel by the lower concentration and higher velocity.

The effect of the total flow rate on the number-average particle size as a function of the axial position along the reactor centerline is presented in Fig. 14. This figure shows a decrease in the particle size as the total Ar flow rate increases. The average particle

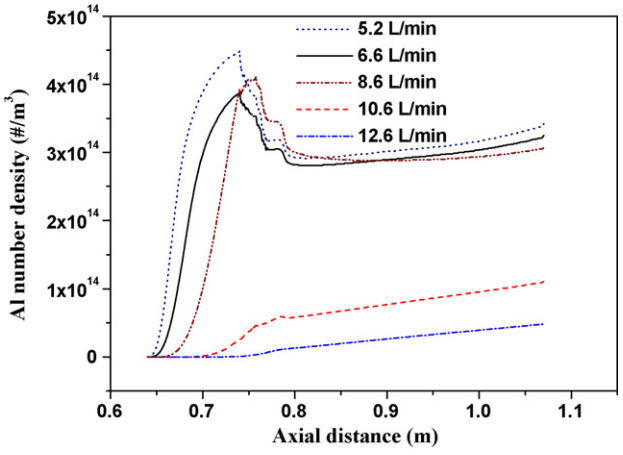

Fig. 13. Al number density along the centerline for different total Ar flow rates.

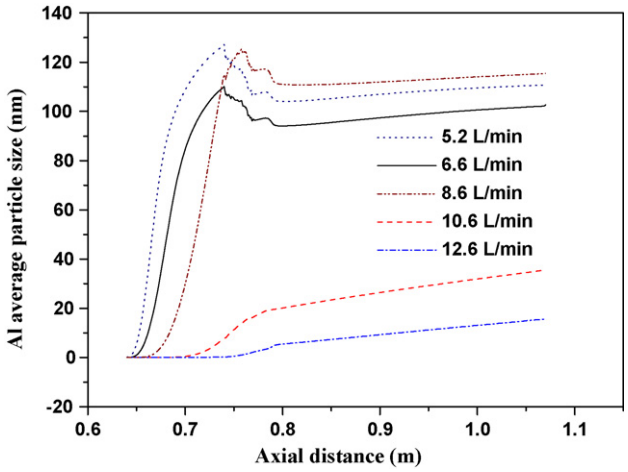

Fig. 14. Al average particle size along the centerline for different total Ar flow rates.

sizes increase before the funnel by particle growth. In the funnel, the average particle sizes decrease here because the nucleation rate is greatly increased in front of the funnel. After the funnel, particle size increases according to the growth mechanism by reaction.

For the total Ar flow rates of 10.6 and 12.6 L/min (25 °C, 86.1 kPa), the average aluminum particle sizes are drastically reduced because of the low concentration and reduced residence time from the higher flow rates. Due to the high velocity and low concentration, aluminum particle nucleation and growth was suppressed and the point of particle nucleation was moved in the direction of the funnel. Particle growth occurs along the small tube by the reaction with the unreacted precursors.

In summary, the best set of nucleation and growth rate constants obtained by the simulation was, respectively, $k_n = 1 \times 10^{-2}$ (m^3/kmol s) at 555 °C (828 K) and $k_g = 2.25 \times 10^5$ (m^4/kmol s) at 873 °C (1146 K). The average particle size decreased with increasing total Ar flow rate due to decreased concentration of the raw materials. It is noted that the concentration effect on the particle size was much greater than the effect of the residence time because of the rapid reaction rates.

The funnel installed inside the reactor provided beneficial effect on the nucleation of the particles by promoting the rapid mixing of gaseous reactants. By changing the total Ar flow rate, the product powder with a specific average particle size can be produced.

4. Summary and conclusions

A 3D CFD simulation was performed with the commercial software Fluent to model and better understand the CVS process for preparing aluminum nanopowder. The results for temperature, velocity profile, and particle size distribution are reasonable. Various operating conditions such as different reactant concentrations and total gas flow rate were tested, which yielded results consistent with experimental data. The particle size computed by simulation showed a good agreement with the experimental results obtained under different operating conditions. Thus, the most important impact of the presented work is that the CFD model can be used to predict the size distribution of Al nanopowders produced under various reaction conditions and to optimize the synthesis process to obtain a desired product. In addition, the visualized internal flow and reaction behaviors provided better understanding of the phenomena taking place inside the reactor. This simulation work could be improved further by using intrinsic nucleation and growth rate parameters, if and when they become available, that would not require estimation by fitting with experimental data.

Acknowledgments

This material is based upon work supported in parts by the University of Utah Funding Incentive Seed Grant Committee and the U.S. DOE Metal Hydride Center of Excellence under Award Number DE-FC36-05GO15069. J.W. Choi thanks the Korean Air Force for granting financial support during his graduate study at the University of Utah. S. Perez-Fontes expresses her gratitude to CONACyT (Consejo Nacional de Ciencia y Tecnología/National Council of Science and Technology) for the scholarship granted to pursue her Ph.D. study at the University of Utah. The authors also wish to acknowledge Fluent. Inc., the provider of the FLUENT® software used in this work. Fluent Inc. is a wholly-owned subsidiary of ANSYS, Inc.

Appendix A. Experimental apparatus

Fig. A1 shows the horizontal CVS system. The diameter of the reactor was 5 cm and a graphite funnel was installed inside the reactor. The system was composed of external entrained-flow powder feeders, reactor and powder collecting system. Carrier Ar streams shown by a and b in Fig. A2 were supplied into the powder feeders to transfer the precursors into the reactor. The flow rate of the carrier Ar was 1 L/min (25 °C, 86.1 kPa) in each stream. Additional carrier Ar with a flow rate of 0.3 L/min (25 °C, 86.1 kPa) was supplied to prevent precursor from sticking in the feed tubes. These flow rates were kept the same for different runs because they were the optimum rates for the feeding of the precursors into the reactor. Dilution Ar gas shown as stream (e) in Fig. A2 was directly supplied into the reactor with various flow rates to control the gaseous reactant concentration. The total Ar flow rate was defined as the sum of all the flow rates (carrier, additional carrier, and dilution Ar flow rates) to the reactor as described in the previous section. The graphite funnel shown in Fig. A3 was placed just at 10 cm behind from the alumina feeding tubes for precursors to increase gas phase mixing. An alumina tube, 0.6 cm inner diameter, was connected to the graphite funnel to improve the contact of gaseous reactants.

Aluminum chloride and magnesium precursors were filled, respectively, in 1.3 cm and 1 cm diameter vial tubes in the glove box and weighed. During heating of the furnace to the target temperature, Ar gas was supplied into the reactor to remove residual oxygen and maintain an inert atmosphere. When the target temperature was reached, the vials filled with precursors were placed in the powder feeders and the feeding rates were set at the desired values. Also, the Ar gas flow for precursor delivery and the dilution Ar flow were set for the experiment. Before collecting the powder, the product powder was passed through the bypass line for 5 min to stabilize the system. After stabilization, the product powder was collected in the main filter and the off-gas from the filter was neutralized in a NaOH solution and vented.

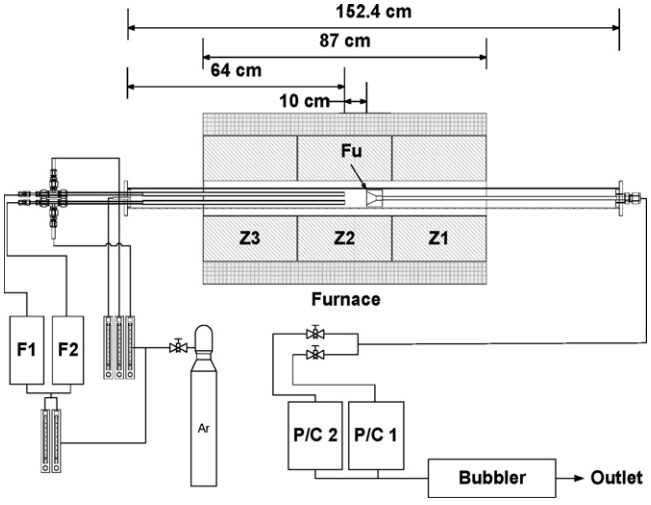

Fig. A1. Modified horizontal experimental apparatus (F1, 2: entrained-flow powder feeders, Fu: graphite funnel, Z1, 2, 3: hot zones, P/C1, 2: powder collectors).

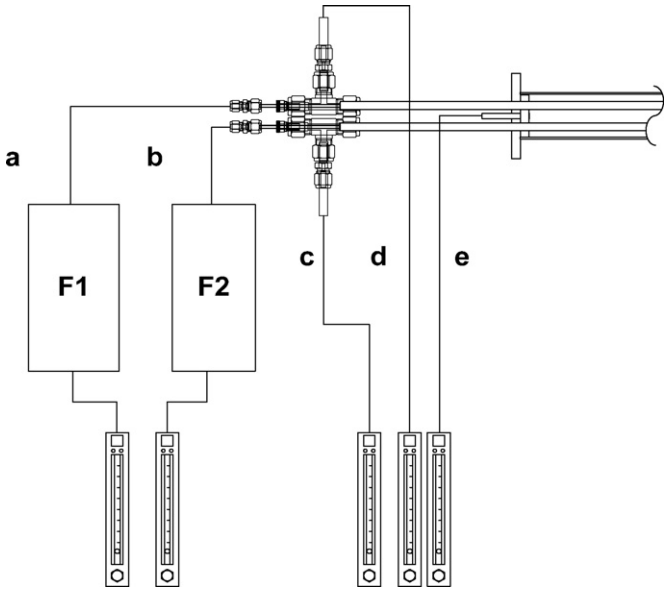

Fig. A2. Detailed view of the Ar inlet area (a, b: carrier Ar; c, d: additional carrier Ar, e: dilution Ar).

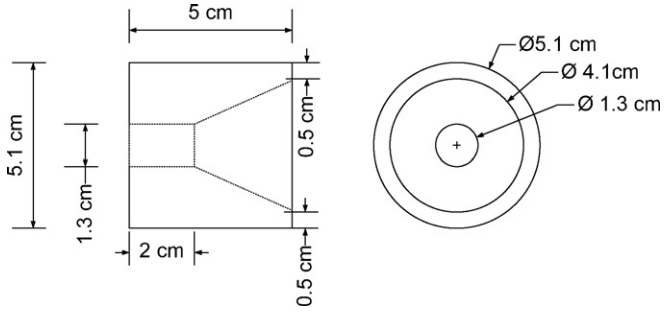

Fig. A3. Detailed view of graphite funnel.

Appendix B. Measured wall temperature profile

The measured profiles for the two different furnaces set at 1000 °C and 1200 °C are shown in Fig. B1.

Appendix C. Derivation of the particle growth rate expression under mass transfer control

The volumetric growth rate of a particle under mass transfer control is given by

$$\frac{dv_p}{dt} = \frac{1}{a} \cdot V_{mol} \cdot \pi L^2 \cdot k_m \cdot (C_{i,b} - C_{i,eq}) \quad \text{(C.1)}$$

where v_p is the particle volume (m^3), a is the stoichiometric coefficient of species i in reaction (1), and the subscripts b and eq represent bulk and equilibrium value, respectively.

The growth rate in terms of the particle diameter is obtained by substituting the expression for the particle volume ($v_p = \pi L^3/6$)

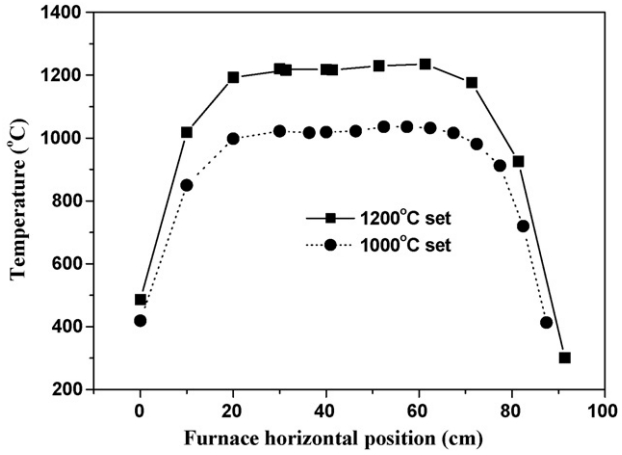

Fig. B1. Temperature profiles of the reactor wall.

into Eq. (C.1), which yields

$$\frac{dd_p}{dt} = \frac{2}{a} \cdot V_{mol} \cdot k_m \cdot C_{i,b} \quad (C.2)$$

Here, it is assumed that the equilibrium concentration of the limiting gaseous reactant at the particle surface is negligible compared with its value in the bulk gas stream, i.e. reaction (1) has a large equilibrium constant (is irreversible).

The mass transfer coefficient, k_m, is calculated based on the assumption that the slip velocity between the gas and the very small particles is zero and thus the Sherwood number becomes

$$Sh = \frac{k_m L}{D_i} = 2.0 \quad (C.3)$$

By substituting Eq. (C.3) into Eq. (C.2), the particle growth rate under mass transfer control is given by

$$G_m = \frac{4}{a} \cdot V_{mol} D_i \frac{m_0}{m_1} C_{i,b} \quad (C.4)$$

where m_0 and m_1 are, respectively, the zeroth (#/m^3) and the first moment (m/m^3) of the particle size distribution, as defined in Eq. (25). Thus, $L = m_1/m_0$ represents the number average particle diameter.

References

[1] G. Sandrock, J. Reilly, J. Graetz, W.-M. Zhou, J. Johnson, J. Wegrzyn, Alkali metal hydride doping of α-AlH_3 for enhanced H_2 desorption kinetics, Journal of Alloys and Compounds 421 (1–2) (2006) 185–189.
[2] B. Bogdanovi, M. Schwickardi, Ti-doped alkali metal aluminium hydrides as potential novel reversible hydrogen storage materials, Journal of Alloys and Compounds 253–254 (1997) 1–9.
[3] J. Lu, Z.Z. Fang, H.Y. Sohn, A new Li–Al–N–H system for reversible hydrogen storage, J. Phys. Chem. B 110 (29) (2006) 14236–14239.
[4] M. Fichtner, O. Fuhr, Synthesis and structures of magnesium alanate and two solvent adducts, Journal of Alloys and Compounds 345 (1–2) (2002) 286–296.
[5] H. Sohn, T. Ryu, J. Choi, K. Hwang, G. Han, Y. Choi, Z. Fang, The chemical vapor synthesis of inorganic nanopowders, Journal of the Minerals, Metals and Materials Society 59 (12) (2007) 44–49.
[6] J.W. Choi, H.Y. Sohn, Y.J. Choi, Z.Z. Fang, Chemical vapor synthesis and characterization of aluminum nanopowder as a precursor of hydrogen storage materials, J. Power Sources 195 (5) (2010) 1463–1471.
[7] V.V. Srdic, M. Winterer, A. Moller, H. Hahn, G. Miehe, Nanocrystalline zirconia surface-doped with alumina: chemical vapor synthesis, characterization, and properties, Journal of the American Ceramic Society 84 (12) (2001) 2771–2776.
[8] H.Y Sohn, S. Paldey, Synthesis of ultrafine nickel aluminum particles by the hydrogen reduction of vapor-phase mixtures of $NiCl_2$ and $AlCl_3$, Journal of Materials Research 13 (11) (1998) 3060–3069.
[9] H.Y. Sohn, S. Paldey, Synthesis of ultrafine particles and thin films of Ni_4Mo by the vapor-phase hydrogen coreduction of the constituent metal chlorides, Materials Science and Engineering A 247 (1–2) (1998) 165–172.
[10] H.Y. Sohn, S. Paldey, Synthesis of ultrafine particles of intermetallic compounds by the vapor-phase magnesium reduction of chloride mixtures. Part I. Titanium aluminides, Metallurgical and Materials Transactions B 29 (2) (1998) 457–464.
[11] H.Y. Sohn, S. Paldey, Synthesis of ultrafine particles of intermetallic compounds by the vapor-phase magnesium reduction of chloride mixtures. Part II. Nickel aluminides, Metallurgical and Materials Transactions B 29 (2) (1998) 465–469.
[12] T. Ryu, H.Y. Sohn, G. Han, Y.-U. Kim, K. Hwang, S. Mena, Z.Z. Fang, Nanograined WC–Co composite powder by chemical vapor synthesis, Metall. Mater. Trans. B 39B (2008) 1–6.
[13] J.W. Choi, Chemical vapor synthesis and characterization of metallic nanopowders relevant to hydrogen storage materials, Ph.D. Dissertation, University of Utah, Salt Lake City, UT, USA, 2009.
[14] S.E. Pratsinis, Simultaneous nucleation, condensation, and coagulation in aerosol reactors, Journal of Colloid and Interface Science 124 (2) (1988) 416–427.
[15] Fluent, Fluent 6.3 User's Guide, Fluent Inc., Lebanon, NH, 2006.
[16] F. Aristizabal, R.J. Munz, D. Berk, Modeling of the production of ultra fine aluminium particles in rapid quenching turbulent flow, Journal of Aerosol Science 37 (2) (2006) 162–186.
[17] D. Mukherjee, A. Prakash, M.R. Zachariah, Implementation of a discrete nodal model to probe the effect of size-dependent surface tension on nanoparticle formation and growth, Journal of Aerosol Science 37 (10) (2006) 1388–1399.
[18] Y. Ji, H.Y. Sohn, H.D. Jang, Wan, T.A. Ring, Computational fluid dynamic modeling of flame reaction process for silica nanopowder synthesis from tetraethylorthosilicate (TEOS), Journal of American Ceramic Society 90 (2007) 3838–3845.
[19] Y. Ji, Computation fluid dynamics simulation of flame spray process for silica nanopowder synthesis from tetraethylorthosilicate (TEOS), M.S. Thesis, University of Utah, Salt Lake City, UT, 2007.
[20] T.T. Kodas, M.J. Hampden-Smith, Aerosol Processing of Materials, Wiley-VCH, New York, 1999, pp. 97–100, 124–127.
[21] S.K. Rhee, Wetting of ceramics by liquid aluminum, Journal of the American Ceramic Society 53 (7) (1970) 386–389.
[22] R.R. Hultgren, Selected Values of the Thermodynamic Properties of the Elements, American Society for Metals, Metals Park, OH, 1973, pp. 25–31.
[23] J. Szekely, J.W. Evans, H.Y. Sohn, Gas–Solid Reactions, Academic Press, New York, 1976, pp. 70–73.
[24] H.Y. Sohn, J. Szekely, A structural model for gas–solid reactions with a moving boundary-IV. Langmuir-Hinshelwood kinetics, Chemical Engineering Science 28 (5) (1973) 1169–1177.
[25] A.D. Randolph, M.A. Larson, Theory of Particulate Processes: Analysis and Techniques of Continuous Crystallization, 2nd ed., Academic Press, Orlando, FL, 1988, p. 32.
[26] R. McGraw, Description of aerosol dynamics by the quadrature method of moments, Aerosol Science and Technology 27 (2) (1997) 255–265.